# Doubly Tuned Exchange-Correlation Functionals for Mixed-Reference Spin-Flip Time-Dependent Density Functional Theory

Konstantin Komarov, Woojin Park, Seunghoon Lee, Miquel Huix-Rotllant, Cheol Ho Choi

# Doubly Tuned Exchange-Correlation Functionals for Mixed-Reference Spin-Flip Time-Dependent Density Functional Theory

Konstantin Komarov,[†,‖] Woojin Park,[‡,‖] Seunghoon Lee,[*,¶] Miquel Huix-Rotllant,[*,§] and Cheol Ho Choi[*,‡]

†*Center for Quantum Dynamics, Pohang University of Science and Technology, Pohang 37673, South Korea*

‡*Department of Chemistry, Kyungpook National University, Daegu 41566, South Korea*

¶*Division of Chemistry and Chemical Engineering, California Institute of Technology, Pasadena, California 91125, USA*

§*Aix-Marseille Univ, CNRS, ICR, Marseille 13397, France*

‖*Contributed equally to this work*

E-mail: slee89@caltech.edu; miquel.huix-rotllant@cnrs.fr; cchoi@knu.ac.kr

**Abstract**

It is demonstrated that significant accuracy improvements of MRSF-TDDFT can be achieved by introducing two different exchange-correlation (XC) functionals for the reference Kohn-Sham DFT and the response part of calculations, respectively. Accordingly, two new XC functionals of doubly tuned Coulomb attenuated method-vertical excitation energy (DTCAM-VEE) and DTCAM-AEE were developed on the basis of the "adaptive exact exchange (AEE)" concept in the framework of the Coulomb-attenuating XC functionals. The values by DTCAM-VEE are in excellent agreement with those of Thiel's set (mean absolute errors (MAEs) and interquartile range (IQR) of 0.218 and 0.327 eV, respectively). On the other hand, DTCAM-AEE faithfully reproduced the qualitative aspects of conical intersections (CIs) of *trans*-butadiene and thymine, and the nonadiabatic molecular dynamics (NAMD) simulations on thymine. The latter functional also remarkably exhibited the exact 1/R asymptotic behavior of the charge-transfer state of an ethylene-tetrafluoroethylene dimer, and the accurate potential energy surfaces (PESs) along the two torsional angles of retinal protonated Schiff base model with six double bonds (rPSB6). Overall, DTCAM-AEE generally performs well, as its MAE (0.237) and IQR (0.41 eV) are much improved as compared to BH&HLYP. The current idea can be also applied to other XC functionals as well as other variants of linear response theories, opening a new way of developing XC functionals.

# TOC Graphic

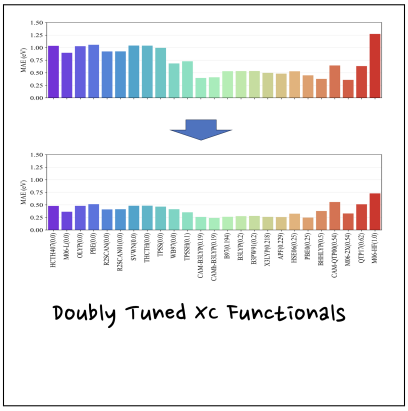

# Introductions

A widely used methodology for studying molecular excited states is the spin-conserving linear response time-dependent density functional theory (LR-TDDFT).[1–3] Despite the success of conventional LR-TDDFT in describing the low-lying excitation energies of molecules, there are well-known limitations. These include the energy of long-range charge transfer excitations within pure and hybrid exchange-correlation (XC) functionals,[4–8] excited states with substantial double excitation character,[9–12] states of molecules undergoing bond breaking,[13,14] and the topology of conical intersections (CIs).[15–18] There have been various attempts to address the issues of the charge-transfer[19,20] and double excitations.[10,21,22] These limitations can be also overcome more explicitly by the spin-flip model,[23] especially the spin-flip (SF)-TDDFT,[24–27] which utilizes spin-flip excitations from high spin triplet reference ($M_s = +1$). Thus, the incorrect description of the CI, single bond-breaking, and the poor description of multireference electronic states, can be corrected by it.[24–26] However, SF-TDDFT may suffers from considerable spin contamination.[28–30] As it is due to the incomplete configurations of its response space, a fundamental solution for the problem is to include the missing ones. However, unlike wave function theories, a considerable challenge remains with respect to TDDFT when going beyond the adiabatic approximation to account for more than single excitations.[21] The introduction of the tensor equation-of-motion (TEOM) formalism yields the spin-adopted (SA) SF-DFT, which is free of spin contamination by expanding electron configurations.[31] However, its analytic energy gradient has yet to be developed due to the inherent complexity of TEOM.

Instead of introducing expensive high-rank excitations from a single reference, two references ($M_s = +1$ and $M_s = -1$ of triplet reference) were adopted as an alternative way of expanding the response space by some of us.[32] To recover the *idempotency* condition of its mixed density,[33] a *hypothetical* single reference by a novel spinor transformation has been introduced, finally yielding a mixed reference (MR) spin-flip (SF)-TDDFT.[32,34] The new approach not only eliminates the problematic spin-contamination pitfalls of SF-TDDFT[26] but also introduces additional multireference features to TDDFT. Like SF-TDDFT, the MRSF-TDDFT also considers the singlet ground state

($S_0$) and other excited states on an equal footing, which not only eliminates the general topological problem[35–37] of CI but also allows the description of open-shell ground singlet states such as diradicals, Jahn-Teller distortion[38,39] as well as bond-breaking.[40] Furthermore, the one-electron spin-flip excitation from the mixed triplet reference includes the important *doubly* excited configuration, which is the main ingredient to properly account for the $CI_{21}$ between bright $1^1B_u^+$ and dark $2^1A_g^-$ states of s-*trans*-butadiene and s-*trans*-hexatriene.[12] Therefore, after its initial introductions, the MRSF-TDDFT[32,34] has proven to be a promising quantum theory for general use, overcoming the major issues of existing theories. In a series of studies,[35–45] it has been demonstrated that the MRSF-TDDFT approach can also yield accurate nonadiabatic coupling matrix elements (NACMEs)[40,41] enabling reliable nonadiabatic molecular dynamics (NAMD) simulations,[44,46–51] accurate spin-orbit couplings (SOC)[52] and very accurate X-ray absorption predictions.[53] This method has also been successfully used in designing highly performing optoelectronic materials.[37,54–56] The MRSF-TDDFT has finally been released publicly by the GAMESS (July 31, 2022 R1 Public Release Version).[57]

As a variant of linear response theory, the performance of MRSF-TDDFT is also subjective to the choice of XC functionals. As was pointed out by Huix-Rotllant et al.,[58] within the widely used collinear (one-component) SF formalism, which is also adopted by MRSF-TDDFT, the configurations obtained by different SF transitions couple through the exact exchange only. It inevitably requires a larger fraction of the exact exchange, such as in the BH&HLYP functional,[38] limiting the choice of XC functionals. Therefore, the main objective of the current study is to explore a way of developing customized XC functionals for MRSF-TDDFT as well as linear response theories in general. Vertical excitation energies (VEEs) may be one of the important criteria for this, which are the properties at Franck-Condon (FC) geometries. In the special applications of NAMD, however, various other parts of potential energy surfaces (PESs) away from FC are frequently encountered. Especially, the CI regions are of utmost importance for the success of NAMD simulations. However, properly established CIs that can be adopted for benchmarks, are scarce in the literature. In the current study, each CI of *trans*-butadiene[12] and thymine[44] shall be adopted. The former and latter have been relatively well established by high-level quantum theories[12] and by

the good agreements between NAMD simulations and various experimental results,[44] respectively. The ethylene-tetrafluoroethylene dimer,[4] as well as retinal protonated Schiff base with six double bonds (rPSB6),[59] shall be also adopted for further verification of the developed XC functionals. While the former is an ideal test system for $r^{-1}$ asymptotic behavior of charge-transfer states, the latter is the critical model of retinal photo-isomerization reactions.

The main focus of the current study is to explore the advantages of "double tuning" or "adaptive exact exchange (AEE)" for individual SCF problem and response parts of MRSF-TDDFT calculations, respectively. It is common and intuitive to employ the same XC functional for the mean-field ground SCF and the response calculations. However, the use of the same XC function for both problems is not strictly necessary, as time-dependent Kohn-Sham stems from a TDDFT time-dependent exchange-correlation action, and Kohn-sham DFT is based on a static (in time) exchange-correlation functional, despite in practice both functionals are approximated by approximate XC functionals. In other words, even if we would use the exact DFT XC functional in the response equations, it would be an approximate functional for TDDFT, since it would only depend on the instantaneous density.[3] In fact, Dreuw and Head-Gordon[60] showed that the errors of TDDFT are coming from both the orbital energies of SCF and response calculations. By individually tuning XC functionals for the two steps, we demonstrated that one can obtain better XC functionals for response theories.

In this regard, the current approach resembles the xDH scheme used in double-hybrid (DH) methods for ground state properties, where all energy terms associated with the DH functionals are evaluated by using the SCF orbitals and corresponding densities from some lower-rung functionals, while a top-rung DH functional is adopted for final energy evaluation for its improved accuracy due to the introduction of the nonlocal correlation effects.[61] The Current study explicitly adopts two different XC functionals in the special cases of excited state properties.

# Theoretical Backgrounds and Computational Details

With the help of dimensional transformation $U^{(k)}$,[34] the singlet and triplet orbital Hessians can be succinctly represented with a single form of:

$$A^{(k)(0)}_{pq,rs} = U^{(k)}_{pq} \left\{ \delta_{pr} F_{qs\beta} - \delta_{qs} F_{pr\alpha} - c_{\mathrm{MRSF}} (pr|sq) \right\} U^{(k)}_{rs}, \tag{1}$$

where $k =$ singlet/triplet and

$$\begin{aligned} F_{pq\alpha} &= h_{pq\alpha} + V^{xc}_{pq\alpha} + \sum_i [2(pq|ii) - c_{\mathrm{HF}}(pi|iq)] \\ &\quad + \sum_x [(pq|xx) - c_{\mathrm{HF}}(px|xq)], \end{aligned} \tag{2a}$$

$$\begin{aligned} F_{pq\beta} &= h_{pq\beta} + V^{xc}_{pq\beta} + \sum_i [2(pq|ii) - c_{\mathrm{HF}}(pi|iq)] \\ &\quad + \sum_x (pq|xx), \end{aligned} \tag{2b}$$

where $c_{\mathrm{HF}}$ and $c_{\mathrm{MRSF}}$ denote the coefficients for the exact Hartree–Fock exchange used in SCF and response calculations, respectively. The $h_{pq\sigma}$ and $(pq|ii)$ are the one- and two-electron integrals, respectively, and $V^{xc}_{pq\sigma}$ represents the matrix elements of the first functional derivatives of the XC functional with respect to electron density. All two-electron integrals are written in chemist notation. We have generally assumed that $c_{\mathrm{MRSF}}$ is equal to $c_{\mathrm{HF}}$.

With the Mixed Reference (MR)-Reduced Density Matrix (RDM) of MRSF-TDDFT, *a posteriori* coupling of $c_{\mathrm{SPC}}$ was introduced[32] as:

$$A'_{pq,rs} = c_{\mathrm{SPC}} \left\langle \Psi^{M_S=+1}_{p\alpha q\beta} \middle| \hat{H} \middle| \Psi^{M_S=-1}_{r\beta s\alpha} \right\rangle, \tag{3}$$

where $c_{\mathrm{SPC}}$ is a set of CO-CO, OV-OV, CO-OV spin-pair coupling parameters (C=closed, O=open, V=virtual MOs), $\left\langle \Psi^{M_S=+1}_{p\alpha q\beta} \right|$ and $\left| \Psi^{M_S=-1}_{r\beta s\alpha} \right\rangle$ are the bra and ket vectors for configurations originating from the $M_S = +1$ and $M_S = -1$ components of the mixed reference state, respectively. We have

also generally assumed that $c_{\mathrm{SPC}}$ is equal to $c_{\mathrm{MRSF}}$. The corresponding equations of gradients are presented in Sections II and III of Supporting Information.

All single-point calculations were performed using a locally modified GAMESS-US program package.[57] Thiel's[62] set was adopted for the reference energies of VEEs with two different all-electron basis sets of 6-31G(d) and cc-pVTZ. This set contains the most common organic chromophores such as polyenes, polyaromatic hydrocarbons, carbonyl compounds, amides, heterocycles, and nucleobases, and is widely used to benchmark existing and new computational methods. We utilized a set of 49 symmetry-labeled singlet excited states as was previously done.[38] In this work, the latest version of the aforementioned set (theoretical best estimate; TBE-2) was used as reference values. The various DFT functionals were employed (the amount of the exact exchange is given in parentheses, where range-separated functionals presented as $\alpha$ (short range), $\beta$ (long range), $\omega$ (range-separation)), i.e., HCTC407(0.0),[63] M06-L(0.0),[64] OLYP(0.0),[65] R2SCAN(0.0),[66] R2SCAN01(0.0),[67] SVWN(0.0),[68,69] THCTH(0.0,[70] TPSS(0.0),[71] $\omega$B97(0.0, 1.0, 0.4)[72], TPSSh(0.1),[73] CAM-B3LYP(0.19, 0.46, 0.33),[74] CAMh-B3LYP(0.19, 0.31, 0.33),[75] B97(0.194),[76,77] B3LYP(0.2),[78–80] B3PW91(0.2),[81] X3LYP(0.218),[82] APF(0.229),[83] HSE06(0.25, -0.25, 0.11),[84] PBE0(0.25),[85] BH&HLYP(0.5),[80] CAM-QTP00(0.54, 0.37, 0.29),[86] M06-2X(0.54),[87] QTP17(0.62)[86] and M06-HF(1.0).[87]

# Results and Discussions

## Vertical Excitation Energy And The Amount of Exact Exchange

Unlike TDDFT, both SF- and MRSF-TDDFT produce a ground singlet ($S_0$) state as one of their response states. The typical ground state of closed-shell systems is mostly described by a single configuration as a result of O2 $\rightarrow$ O1 spin-flip excitation in Fig. 1(a). As the difference of the Kohn-Sham orbital energies is the leading term of the diagonal elements of the A matrix, the VEEs and the energy gaps of $S_x - S_0$ ($x \geq 1$) of both SF- and MRSF-TDDFT can be largely proportional to the O2 - O1 gap.[88,89] The linear relation between them with the amount of the exact exchange contribution is presented in the case of *trans*-butadiene (See Fig. 1(b)), where it is clearly seen that

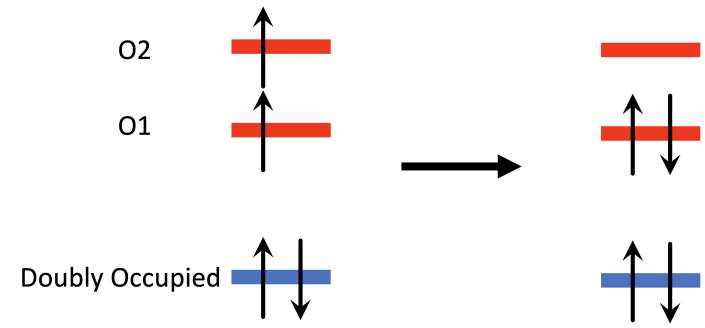


(a)

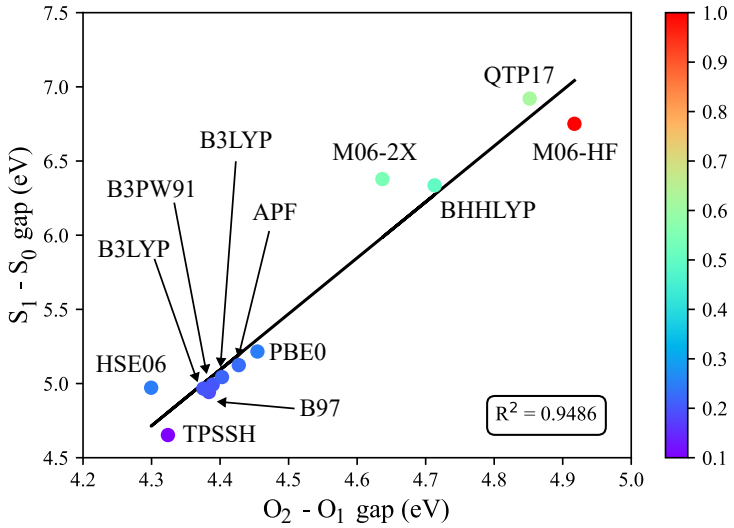


(b)

Figure 1: (a) Spin-flip excitation for the closed-shell ground state by MRSF-TDDFT. (b) The VEEs between $S_1$ and $S_0$ states with respect to Kohn-Sham orbital energy differences between O2 and O1 for several functionals in *trans*-butadiene as calculated with MRSF-TDDFT/6-31g(d) basis set. Note that the color represents the amount of exact exchange contribution.

the O2 - O1 gap, as well as VEEs, are proportional to the amount of exact exchange. The collinear formalism of MRSF-TDDFT inevitably requires a larger fraction of the exact exchange to produce correct response states, such as in the BH&HLYP functional, which tends to overestimate VEEs. This seemingly contradictory condition may be alleviated by the introduction of an AEE concept, where individual XC functionals with different amounts of exact exchange are designed for orbital optimization and linear response steps of MRSF-TDDFT calculations.

More specifically, the overall process is composed of two consecutive steps: (i) high spin triplet KS-DFT orbital optimizations by the XC functional with $c_{HF}$ producing the Eq. 2, and (ii) the matrix element computations of orbital Hessian by another XC functional with $c_{MRSF}$=$c_{SPC}$. If $c_{HF}$ is equal to $c_{MRSF}$=$c_{SPC}$, the two steps are processed by the same XC functional. Otherwise, it can be considered that two different XC functionals are utilized for them, respectively. In reality, it is noted that the collinear formulation of the current MRSF-TDDFT eliminates the pure XC functional contributions during the response part of the calculation. It should be emphasized that the current approach is consistent with the previous implementation of analytic gradients for MRSF-TDDFT. As the modification is as simple as separating $c_{HF}$ into $c_{HF}$ and $c_{MRSF}$, minimal changes to the analytic gradient formulations were needed. The specific corrections are available in the Sections II and III of Supporting Information.

## Performance Analysis of Adaptive Exact Exchange

Mean absolute errors (MAEs), as well as boxplots of predicted VEEs by various XC functionals as compared to the reference values, are presented in Fig. 2 and 3, respectively, where the XC functionals are listed in the X-axis with the increasing order of exact exchange contributions. In the typical case of $c_{MRSF} = c_{SPC} = c_{HF}$ as shown in the top of Fig. 2, the BH&HLYP and M06-2X, which have $c_{HF}$ = 0.5 and 0.54, exhibit the smallest MAE of 0.379 and 0.358 eV, respectively. Noticeably, the two Coulomb attenuated functionals of CAM-B3LYP and CAMh-B3LYP also exhibit relatively small MAEs of 0.398 and 0.41 eV, respectively. The two CAM functionals have variable exact exchange contributions as a function of distance up to 65% (CAM) and 50% (CAMh) in the asymptotic region. Generally, the MAEs of other XC functionals are increasing, as $c_{HF}$ is either smaller than 0.19 or higher than 0.5. A similar trend of MAEs was also seen in the case of LR-TDDFT.[38]

In order to investigate the effect of AEE, a special setting of $c_{MRSF} = c_{SPC} = 0.5$, which mimics the BH&HLYP functional, (more specifically its exact exchange component), was adopted regardless of $c_{HF}$. As a result, while the SCF part is performed with the regular XC functionals,

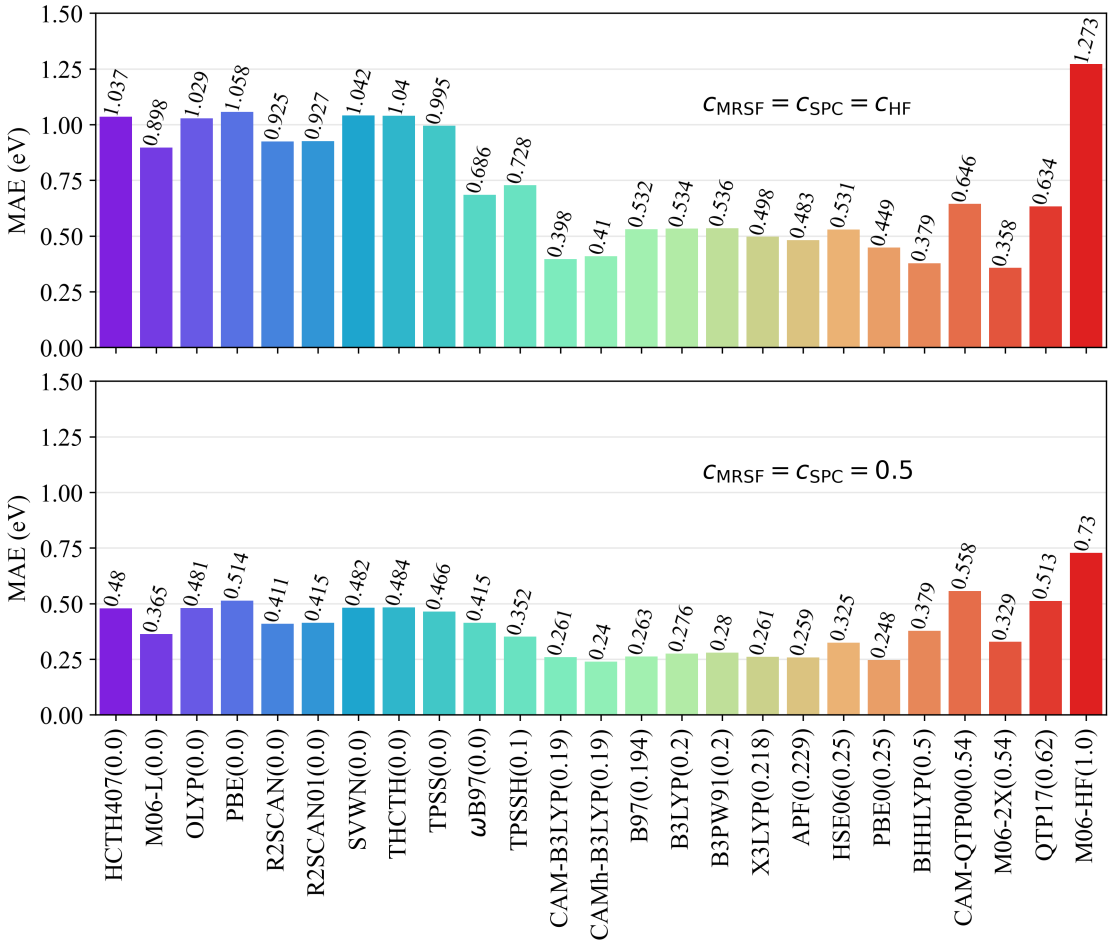


Figure 2: The MAEs (in eV) of the $S_1$ and $S_2$ excited states based on symmetry label compared with TBE-2 for Thiel's molecular set as a function of XC functionals, where top figure represents the MAE results with $c_{MRSF}$=$c_{SPC}$=$c_{HF}$, while the bottom figure were generated with $c_{MRSF}$=$c_{SPC}$=0.5. All calculations were done by MRSF-TDDFT with 6-31G(d) basis set. The values in parentheses are $c_{HF}$ for each functional. It should be noted that the actual percentage of $c_{HF}$ of $\omega$B97, CAM-B3LYP and CAMh-B3LYP are 0.0 $\sim$ 1.0, 0.19 $\sim$ 0.65 and 0.19 $\sim$ 0.50, respectively. (see Table 1) The collinear formulation of the current MRSF-TDDDFT eliminates the contribution of pure XC functionals of VWN5 and LYP. The corresponding table with cc-pVTZ basis set is presented in Section I of Supporting Information.

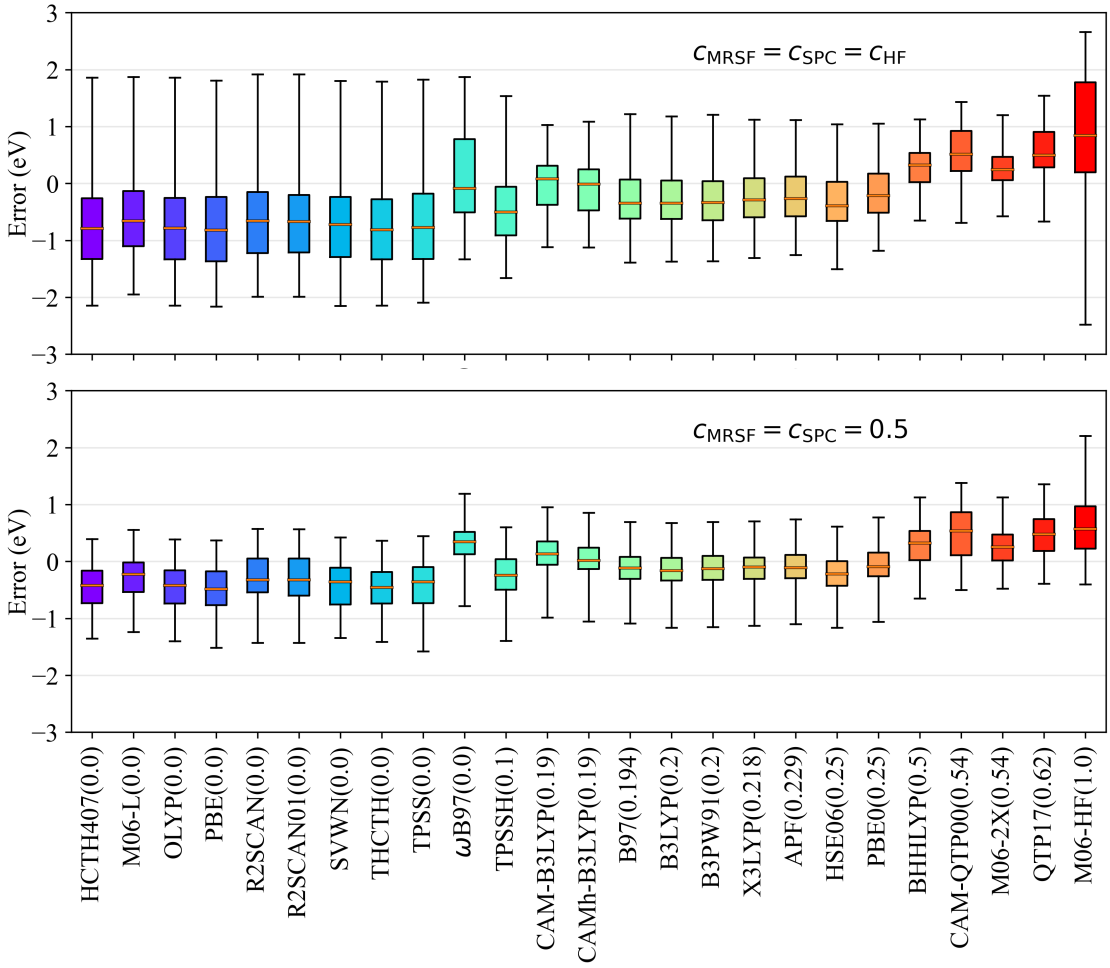


Figure 3: The boxplot (medians, interquartile ranges, as well as wiskers) of the $S_1$ and $S_2$ excited state error (in eV) compared with TBE-2 for Thiel's molecular set as a function of XC functionals, where top figure utilize $c_{MRSF}$=$c_{SPC}$=$c_{HF}$, while the bottom figure utilizes $c_{MRSF}$=$c_{SPC}$=0.5. All calculations were done by MRSF-TDDFT with 6-31G(d) basis set. The values in parentheses are $c_{HF}$ for each functional. The values in parentheses are $c_{HF}$ for each functional. It should be noted that the actual percentage of $c_{HF}$ of $\omega$B97, CAM-B3LYP and CAMh-B3LYP are 0.0 $\sim$ 1.0, 0.19 $\sim$ 0.65 and 0.19 $\sim$ 0.50, respectively. (see Table 1) The collinear formulation of the current MRSF-TDDDFT eliminates the contribution of pure XC functionals of VWN5 and LYP. The corresponding table with cc-pVTZ basis set are presented in Section I of Supporting Information.

the modified exact exchange is utilized for the response part of computations.

Remarkably, dramatic reductions (factor of two) of MAEs are achieved in all XC functionals (see bottom of Fig. 2). The XC functionals with $c_{\mathrm{HF}} \sim 0.2$ such as B97, B3LYP, B3PW91, X3LYP, APF, and PBE0 are especially well improved, making their MAEs smaller than that of full BH&HLYP. The smallest MAE of 0.24 eV is achieved by the CAMh-B3LYP. The statistical analysis in the form of boxplots on the same data is shown in Fig. 3, where the improved median and reduction of interquartile ranges (IQR) range are also seen from all XC functionals. For example, the -0.35 (median) and 0.68 (IQR) eV of B3LYP are reduced to -0.16 and 0.39 eV, respectively. In short, the statistical analysis revealed the dramatic impact of AEE on the accuracy of VEE predictions. Especially, it is remarkable to observe that the prediction accuracy of all functionals is improved by the fixed value of $c_{\mathrm{MRSF}} = c_{\mathrm{SPC}} = 0.5$, which shall be further investigated in the subsequent sections.

## New XC functionals of DTCAM-VEE and DTCAM-AEE

As the idea of applying fixed values (0.5) for $c_{\mathrm{MRSF}}$ and $c_{\mathrm{SPC}}$ generally improves the prediction accuracy of VEEs, it would be interesting to further optimize the $c_{\mathrm{MRSF}}$ and $c_{\mathrm{SPC}}$. The Coulomb-attenuating XC functional approach[74] of Eq. 4 is adopted for this.

$$\frac{1}{r_{12}} = \frac{1-[\alpha_i+\beta_i \cdot erf(\mu r_{12})]}{r_{12}} + \frac{\alpha_i+\beta_i \cdot erf(\mu r_{12})}{r_{12}}, \tag{4}$$

where $\alpha_i$, $\beta_i$ and $\mu$ are parameters. While the $\mu$ is set to 0.33 (the same as in CAM(h)-B3LYP functional) in the current study, the $\alpha_i$ and $\beta_i$ are adjusted. Note that subscript $i$ is introduced here to represent the "adaptive" aspect of current proposals. Normally, the subscript $i$ is unnecessary, as the same $\alpha$ and $\beta$ are utilized for both SCF ($i$=1) and response parts ($i$=2) of computations. In the case of CAMh-B3LYP, the $\alpha_1$ and $\beta_1$ are 0.19 and 0.31, respectively and the corresponding values for $\alpha_2$ and $\beta_2$ are identical. (See Table 1)

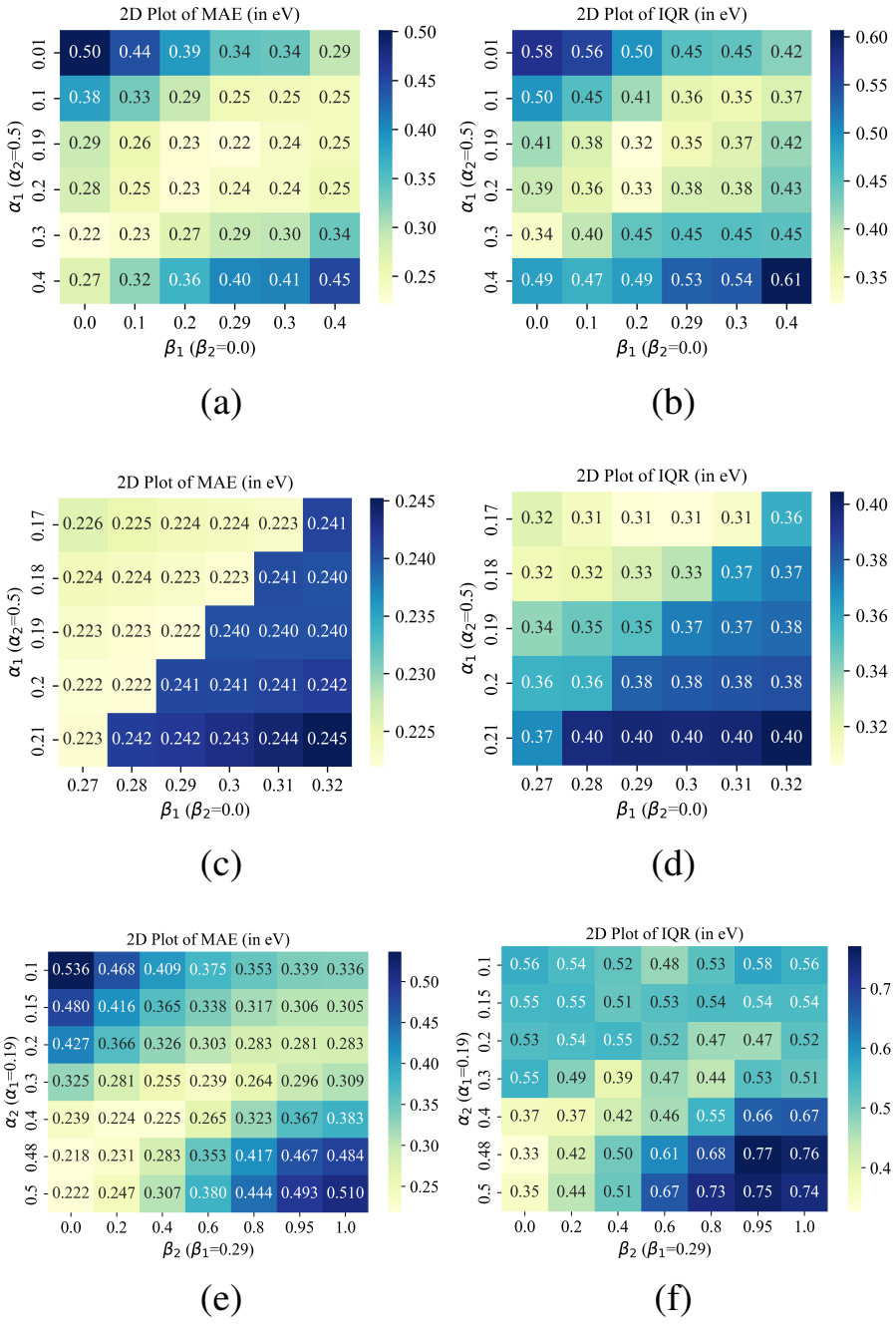


Figure 4: The 2D plot of MAE and IQR (in eV) compared with the TBE-2 of Thiel's. Panel (a) and (b) represent the MAEs and IQRs with $\alpha_1 = 0.4 \sim 0.01$ and $\beta_1 = 0.0 \sim 0.4$ at fixed $\alpha_2$=0.5 and $\beta_2$=0.0, respectively. Panel (c) and (d) represent the MAEs and IQRs with $\alpha_1 = 0.21 \sim 0.17$ and $\beta_1 = 0.27 \sim 0.32$ at fixed $\alpha_2$=0.5 and $\beta_2$=0.0, respectively. Panel (e) and (f) represent the MAEs and IQRs with $\alpha_2 = 0.5 \sim 0.1$ and $\beta_2 = 0.0 \sim 1.0$ at fixed $\alpha_1$=0.19 and $\beta_1$=0.29, respectively. Benchmarks include 49 symmetry-labeled excited states. All calculations were done by MRSF-TDDFT with the 6-31G(d) basis set.

**Table 1: Summary of the exchange–correlation functionals. It should be emphasized that the collinear formulation of the current MRSF-TDDFT eliminates the pure XC contributions of VWN5 and LYP during the response part of calculations.**

| Name | Exchange functional | SCF Part $\alpha_1$ | $\alpha_1 + \beta_1$ | Response Part $\alpha_2$ | $\alpha_2 + \beta_2$ | Correlation functional |
|---|---|---|---|---|---|---|
| CAM-B3LYP | Becke88 | 0.19 | 0.65 | 0.19 | 0.65 | 0.19 VWN5 + 0.81 LYP |
| CAMh-B3LYP | Becke88 | 0.19 | 0.50 | 0.19 | 0.50 | 0.19 VWN5 + 0.81 LYP |
| DTCAM-VEE | Becke88 | 0.19 | 0.48 | 0.48 | 0.48 | 0.19 VWN5 + 0.81 LYP |
| DTCAM-AEE | Becke88 | 0.19 | 0.48 | 0.15 | 1.10 | 0.19 VWN5 + 0.81 LYP |

According to the previous statistical analysis, the combination of CAMh-B3LYP ($\alpha_1$=0.19, $\beta_1$=0.31) for SCF and $c_{\mathrm{MRSF}} = c_{\mathrm{SPC}} = 0.5$ ($\alpha_2$=0.5, $\beta_2$=0.0) for response computations, produces the smallest MAE of 0.24 eV. With the given $\alpha_2$=0.5, $\beta_2$=0.0, both MAE and IQR range are calculated for the range of $\alpha_1$=0.01 $\sim$ 0.4 and $\beta_1$=0.0 $\sim$ 0.4 and the results are presented in the Fig. 4(a) $\sim$ (d). Note that the results obtained with the larger cc-pVTZ basis sets demonstrate similar behavior and yield minimal errors in the same range of $\alpha_1$ and $\beta_1$ (see for detail Section I of Supporting Information). The lowest MAE of 0.222 eV with a rather small IQR range of 0.35 can be achieved with the set of $\alpha_1$=0.19, $\beta_1$=0.29, which was further utilized in the search for optimum $\alpha_2$ and $\beta_2$ as shown in Fig. 4(e) and (f). Both MAE and IQR are slightly improved to 0.218 and 0.327 eV, respectively at $\alpha_2$=0.48, $\beta_2$=0.0. Together, this combination is denoted as DTCAM-VEE (see Table 1 and Fig. 5a), where DT stands for "Doubly Tuned".

As discussed above, the DTCAM-VEE is strictly based on the VEE, which is the property at the FC geometries. Considering excited state PESs and NAMD simulation, FC represents just a single structure when the initial photon is absorbed. There are many other areas of PESs that are equally important. One of the most important structures is certainly the CIs.[90,91] They are molecular geometries at which two (or more) adiabatic electronic states of the molecule become degenerate, which is critically affected by the choice of XC functionals. As the intersecting electronic states at a CI are coupled by the nonvanishing nonadiabatic coupling, CIs provide efficient funnels for the state-to-state population transfer mediated by the nuclear motion. In addition to the CIs, the minima of excited states are also important in determining the decay lifetimes.[44] As discussed in the introduction, each CI and excited state minima between the first and second excited states of

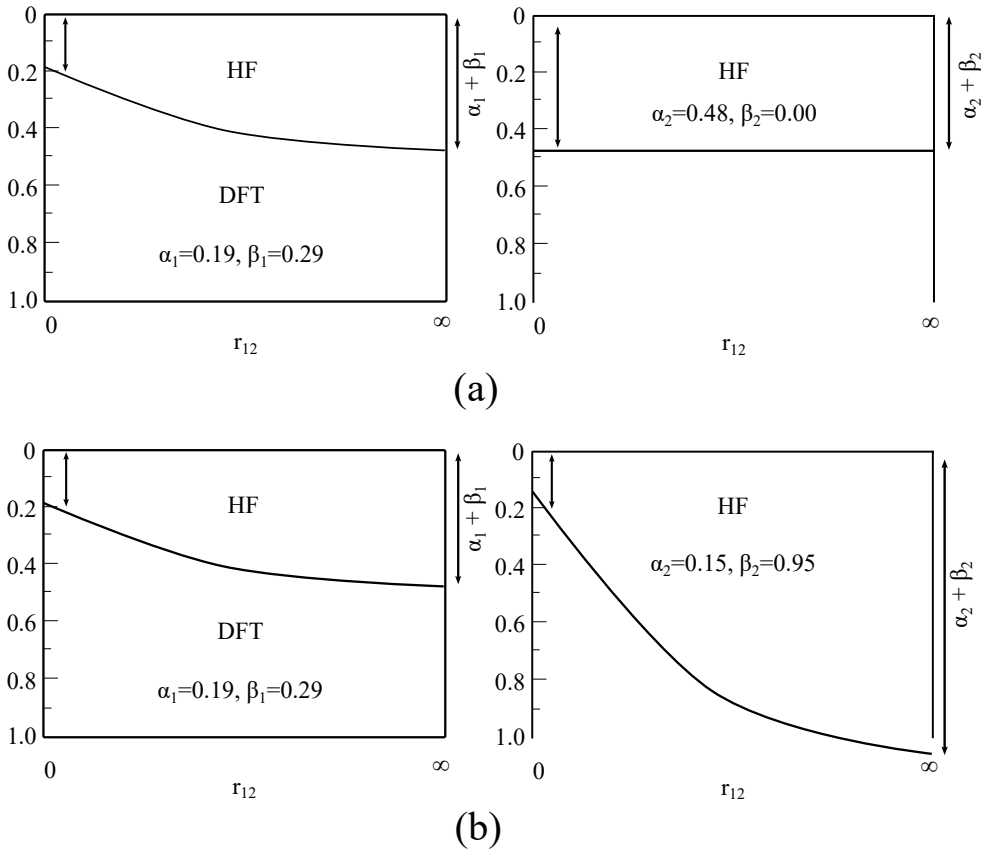


Figure 5: Schematic plots of the exact exchange contributions along $r_{12}^{-1}$ for (a) DTCAM-VEE and (b) DTCAM-AEE.

*trans*-butadiene[12] and thymine[44] were adopted. Short NAMD simulations on thymine were also performed to study the effect of new XC functionals on the decay lifetimes.

According to Fig. 4(e), the MAE is generally lower in the diagonal region (from $\alpha_2$=0.5,$\beta_2$=0.0 to $\alpha_2$=0.1,$\beta_2$=1.0), which was utilized in the search for the optimum $\alpha_2$ and $\beta_2$ combinations. Rather than adopting quantitative criteria such as VEE values, a new XC functional of DTCAM-AEE was established on the basis of qualitative features of the CIs, minima as well as NAMD results (see Table 1 and Fig. 5(b)). The specific detailed reasoning behind each case shall be discussed below. In general, the $\alpha_2$ and $\beta_2$ are fitted to reproduce the entire potential energy surfaces of $S_1$ and $S_2$ near their conical intersections of *trans*-butadiene and thymine. It is noted that DTCAM-AEE has exceptionally large $\beta_2$=0.95, which turned out to be important for the correct 1/r asymptotic behavior of the charge transfer state. (See the charge transfer state section below.) It should be emphasized that DTCAM-AEE generally performs better than BH&HLYP as its MAE and IQR are 0.237 and 0.41 eV, respectively, which are slightly worse than those of DTCAM-VEE (0.218 and 0.32 eV).

## Conical Intersection of *trans*-Butadiene

All-trans polyenes, which have the $1^1B_u^+$ (optically bright) and the $2^1A_g^-$ (optically dark) states at FC geometries,[92–94] are the most prototypical systems of $\pi \rightarrow \pi^*$ excitations. The ionic $1^1B_u^+$ state comprises a one-electron HOMO (highest occupied molecular orbital) $\rightarrow$ LUMO (lowest unoccupied molecular orbital) transition.[95–99] On the other hand, the multi-configurational $2^1A_g^-$ state[92–94,100] is dominated by the HOMO-1 $\rightarrow$ LUMO and HOMO $\rightarrow$ LUMO+1 one-electron and HOMO$^2$ $\rightarrow$ LUMO$^2$ two-electron transitions. The radically different nature of the two states makes its correct description difficult. The corresponding internal conversion (IC) between the $1^1B_u^+$ and the $2^1A_g^-$ states[92–94] has long been argued[101–104] to occur through a true crossing between their PESs. After the $\pi \rightarrow \pi^*$ transition to $1^1B_u^+$, the crossing is reached along the bond length alternation (BLA) displacement mode.[95–99,102,104,105] In a recent study on s-*trans*-butadiene and s-*trans*-hexatriene with various quantum chemical theories,[12] the $1^1B_u^+ < 2^1A_g^-$ state ordering

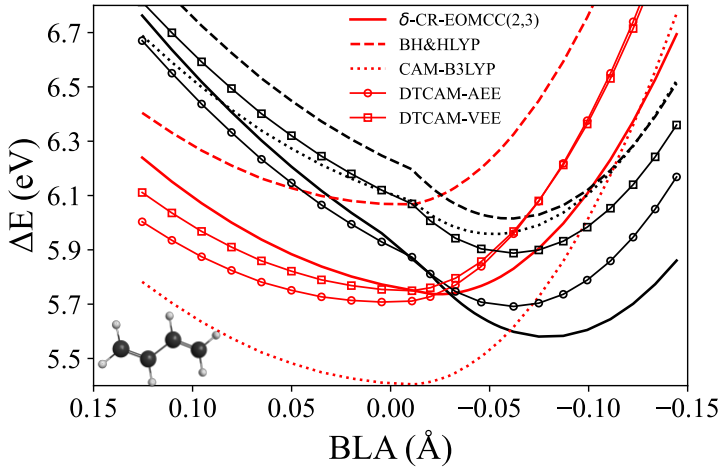


(a)

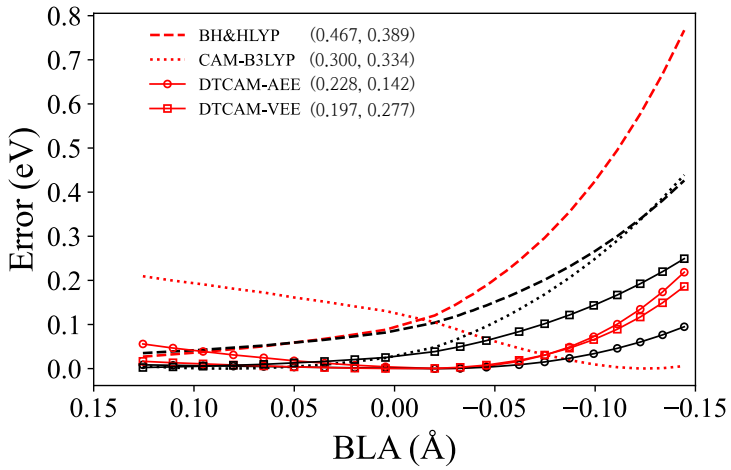


(b)

Figure 6: (a) The $1^1B_u^+$ (red) and $2^1A_g^-$ (black) energy profiles along the BLA coordinates of *trans*-butadiene by MRSF-TDDFT/6-31G(d) with BH&HLYP, CAM-B3LYP, DTCAM-AEE and DTCAM-VEE. The values of $\delta$-CR-EOMCC(2,3) with cc-pVTZ basis set from Ref. 12 are also included. The BLA coordinate is defined as the difference between the average length of single bonds and the average length of double bonds. The molecular structure from Ref. 12 is given in the inset. (b) It shows the squared difference of each point with respect to $\delta$-CR-EOMCC(2,3) values. The root mean squared errors for $1^1B_u^+$ and $2^1A_g^-$ states are given in parentheses.

at the FC geometry and the existence of the planar $1^1B_u^+/2^1A_g^-$ curve crossing at the BLA $\approx$ -0.029 $\sim$ -0.032 Å were established. With the explicit inclusion of the doubly excited electronic configurations, the MRSF-TDDFT method was able to recover the correct state ordering and the shapes of the excited state curves. The same PESs were computed by BH&HLYP, CAM-B3LYP, DTCAM-VEE as well as DTCAM-AEE and the results are shown in Fig. 6(a), where the curve by $\delta$-CR-EOMCC(2,3) serves as a reference. The two surfaces of BH&HLYP are generally higher than those of $\delta$-CR-EOMCC(2,3) by $\sim$ 0.3 eV, although the crossing point of BLA = -0.026 is nearly identical. On the other hand, the bright state by CAM-B3LYP is too low, yielding a too-late crossing of BLA = -0.10 Å. Considering overall agreements with the $\delta$-CR-EOMCC(2,3), DTCAM-VEE yields improved PESs. However, the corresponding state crossing occurs at -0.05 Å, which is somewhat different from those of $\delta$-CR-EOMCC(2,3) and BH&HLYP. On the other hand, the dark $2^1A_g^-$ curve is especially further improved by DTCAM-AEE with the reasonable crossing position at BLA = - 0.33 Å. Squared difference plots and RMSDs of each state are presented in Fig. 6(b), where the clearly improved $2^1A_g^-$ by DTCAM-AEE as compared to that of DTCAM-VEE is seen especially after the CI region.

## Conical Intersection and Nonadiabatic Molecular Dynamics of Thymine

Theoretical simulations on the excited state dynamics of thymine agree on the involvement of two excited states relevant for the IC back to the $S_0$ state;[106,107] namely, the optically bright $S_2$ state (characterized by a $\pi \rightarrow \pi^*$ orbital transition) and the dark $S_1$ state ($n \rightarrow \pi^*$ orbital transition). The controversy regarding its excited state mechanism with characteristic slow dynamics has been a subject of debate for a long time,[108–119] which was recently resolved by the NAMD study[44] in combination with MRSF-TDDFT/BH&HLYP. This study supports the $S_1$-trapping mechanism with two lifetimes of $\tau_1$=30$\pm$1 fs ($S_2 \rightarrow S_1$) and $\tau_2$=6.1$\pm$0.035 ps ($S_1 \rightarrow S_0$). The former timescale is quantitatively consistent with the recent time-resolved X-ray[120] ($\tau_1 = 60 \pm 30$ fs) and photoelectron experiments[121]($\tau_1$=37 fs), while the latter slow timescale has been experimentally well documented.[110–119] Therefore, the excited state PESs as well as the NAMD results by BH&HLYP

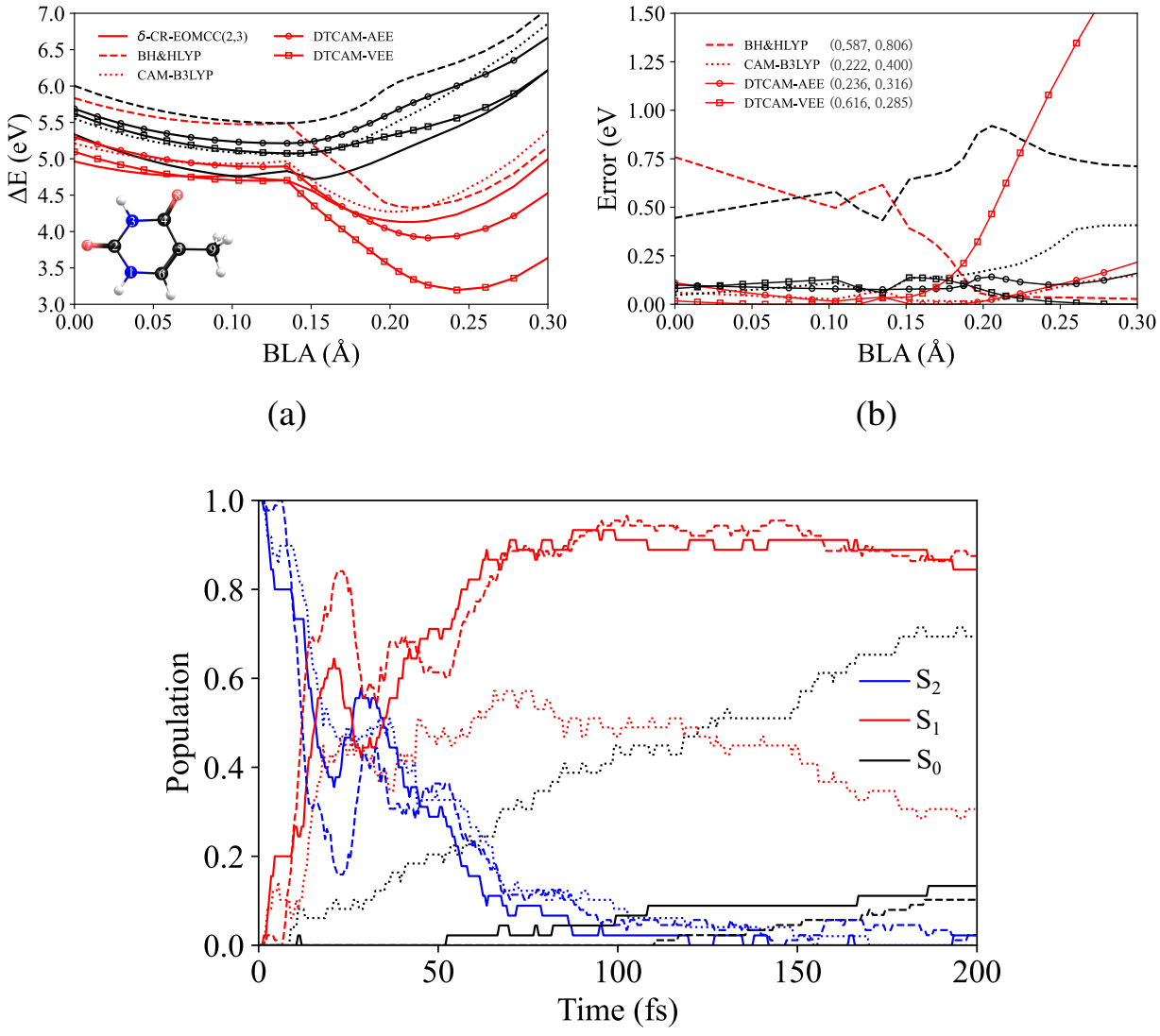


Figure 7: (a) The $S_1$ (red) and $S_2$ (black) energy profiles along the BLA coordinates of thymine by $\delta$-CR-EOMCC(2,3) with cc-pVDZ basis set and MRSF-TDDFT/6-31G(d) with BH&HLYP, CAM-B3LYP, DTCAM-AEE and DTCAM-VEE. The BLA coordinate is defined as the difference between the average increments of the lengths of the double bonds and the decrease of the single bond, BLA $= \frac{1}{2}(\Delta R_{C_4=O_8} + \Delta R_{C_5=C_6}) - \Delta R_{C_4-C_5}$, where $\Delta R$'s are displacements with respect to the $S_0$ equilibrium geometry. The molecular structure with atom numbering from Ref. 44 is given in the inset. (b) It shows the squared difference of each point with respect to $\delta$-CR-EOMCC(2,3) values. The root mean squared errors for $S_1$ and $S_2$ states are given in the parentheses. (c) Time evolutions of the adiabatic $S_0$ (black), $S_1$ (red), and $S_2$ (blue) populations during the NAMD simulations by 6-31G(d) with DTCAM-AEE (solid lines) and DTCAM-VEE (dotted lines) in combination with MRSF-TDDFT. The results of BH&HLYP taken from Ref. 44 are given in dashed lines for comparison.

functionals can serve as a reference. A detailed description of NAMD simulations performed in the current study is presented in Section IV of Supporting Information. It was shown[44] that the PESs around the CI between $S_1$ and $S_2$ ($CI_{21}$) along the BLA motion critically affects the NAMD simulations. The same $S_1$ and $S_2$ surfaces along the BLA of thymine were calculated by CAM-B3LYP, DTCAM-VEE as well as DTCAM-AEE and the results are presented in Fig. 7(a). Unlike in the case of *trans*-butadiene, CAM-B3LYP generally performs well as compared to $\delta$-CR-EOMCC(2,3). The $S_1$ by DTCAM-VEE is about 0.54 eV lower than that of BH&HLYP at FC, while it is about 1.0 eV lower near $S_{1,min}$. On the other hand, the reduction of $S_2$ surface is relatively constant along the entire PES. The significantly stabilized $S_1$ after the CI is clearly seen in the squared difference plots (squared red line) of Fig. 7(b). Consequently, the selectively stabilized $S_{1,min}$ by DTCAM-VEE accelerates the IC $S_1 \rightarrow S_0$ in our NAMD simulations as shown in Fig. 7(c), where $S_0$ population (dotted line) increases rapidly as compared to that of BH&HLYP, producing half of $S_0$ populations in about 100 fs.

On the other hand, it is seen that the $S_1$ and $S_2$ states by DTCAM-AEE are quite consistent with those of $\delta$-CR-EOMCC(2,3). Also, the $S_1$ by DTCAM-AEE is constantly lower than that of BH&HLYP throughout the entire region, without the over-stabilization of $S_{1,min}$. As a result, the population changes by DTCAM-AEE (dashed line in Fig. 7(c)) are quite consistent with those by BH&HLYP (solid line).

## Charge-Transfer State of Ethylene-Tetrafluoroethylene Dimer

As discussed in the introduction, one of well-known failures of LR-TDDFT is the poor description of long-range charge transfer excitations, which is well illustrated in the charge-transfer state of Ethylene-Tetrafluoroethylene dimer (see Fig. 8).[4–8] The origin of the problem is the approximate XC functionals which, in general, do not exhibit the correct 1/R asymptotic behavior (R is the distance between the molecules). MRSF-TDDFT also suffers from the same issue, as MRSF-TDDFT curves calculated with BH&HLYP and DTCAM-VEE exhibit an asymptotic behavior of $\sim$ 0.5/R and 0.48/R, respectively in the relative energy of E(R)-E(4.0 Å) (Fig. 8(a)). The CAM-B3LYP and

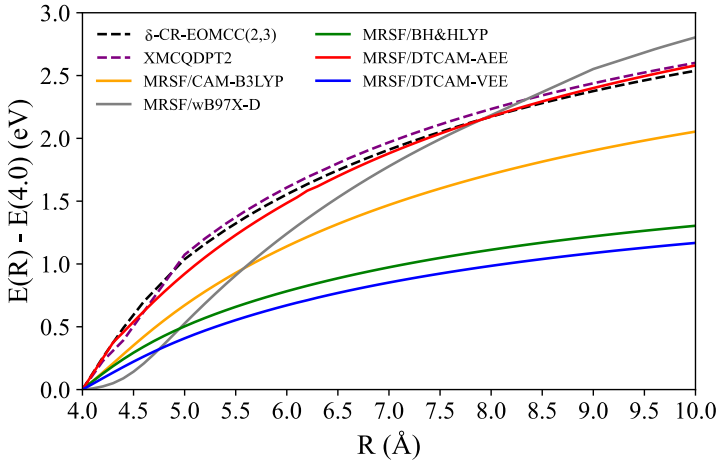


(a)

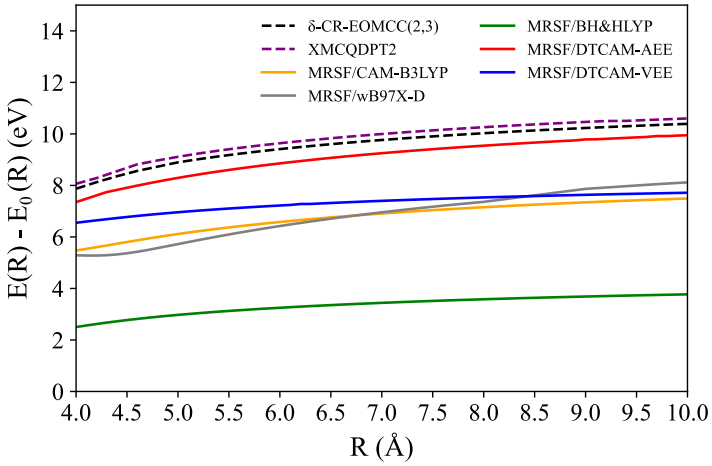


(b)

Figure 8: (a) The relative energies with respect to E(4.0 Å) and (b) $E_0$(R Å) of the lowest CT state of the ethylene-tetrafluoroethylene dimer along the intermolecular distance coordinate (R, distance between center of mass of each molecule) computed by $\delta$-CR-EOMCC(2,3) (black dashed line), three state XMCQDPT2/cc-pVDZ on top of 3SA-CASSCF(4,4)/cc-pVDZ (purple square dotted line), MRSF/6-31G(d) with CAM-B3LYP (orange solid line), wB97X-D (gray solid line), BH&HLYP (green solid line), DTCAM-AEE (red solid line), DTCAM-VEE (blue solid line). The ethylene and tetrafluoroethylene are separately optimized on the ground state using MRSF/6-31G(d)/BH&HLYP method and are used for all calculations.

$\omega$B97X-D improve it with $\sim$ 0.8/R and 1/R. However, the latter is not properly follow 1/R curve well. On the other hand, the relative energies of E(R)-E(4.0 Å) by both $\delta$-CR-EOMCC(2,3) and second-order extended multiconfiguration quasi-degenerate perturbation theory (XMCQDPT2) have the correct 1/R asymptotic behavior. Remarkably, DTCAM-AEE, where the especially large value of $\beta_2$ = 0.95 for the long-range part shows nearly perfect 1/R asymptotic behavior in Fig. 8(a). DTCAM-AEE also exhibits a high accuracy of absolute state energies as it is slightly lower than those of $\delta$-CR-EOMCC(2,3) and XMCQDPT2 in Fig. 8(b). The MRSF-TDDFT with DTCAM-VEE, BH&HLYP as well as both of CAM-B3LYP and $\omega$B97X-D underestimates it. Therefore, it is demonstrated that the 1/R asymptotic behavior with high accuracy can be recovered by adopting a large exact exchange for the long-range within the "adaptive exchange" idea, providing a new direction for developing XC functionals for CT states. This also implies that new functionals can also produce better ionization potentials and electron affinities.

In this context, extended Koopmann approach can be adopted,[42] where some of us showed that it can recover the Dyson orbitals (DO) and its corresponding orbital energies through ionization potential/electron affinity calculations, which shall be explored in the future. A calculation on thymine already shows a promising performance of DTCAM-AEE, as it reproduces highly accurate IP as compared to experiment (See Table S1) of Supporting Information.

## Conical Intersections of Protonated Schiff Base

Retinal photoisomerization is at the heart of the vision process of rhodopsins, involving an ultrafast nonadiabatic transition between $S_1$ and $S_0$ via a CI. Due to the size of the retinal, to determine the impact of electron correlation treatment, various truncated models of the protonated Schiff base (PSB) have been exhaustively studied,[59,123–126] where multireference wave function methods have often been the most successful methods to describe the complex intersection topologies and energetic barriers in the excited states.[16,17,127–132] For the present study, a model of the largest rPSB6 is adopted and extended multi-state second-order complete-active space perturbation theory (XMS-CASPT2) is serving as a good reference for testing the quality of adaptive-exchange XC

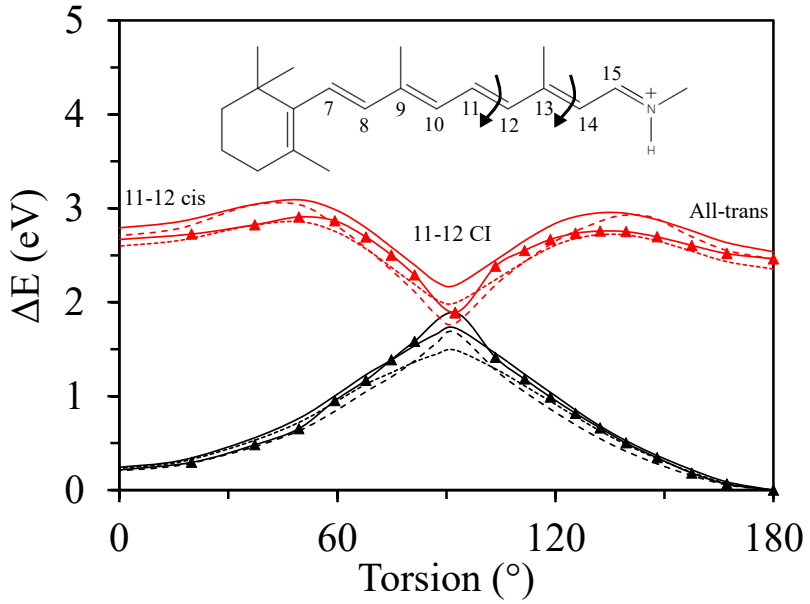


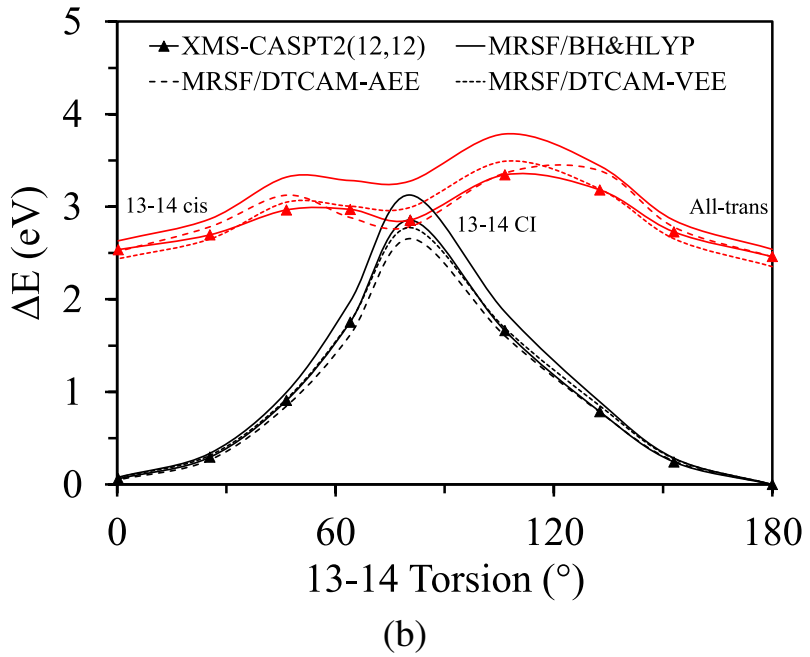


Figure 9: (a) and (b) represent the 11-cis and 13-cis torsional pathways of the $S_0$ (black) and $S_1$ (red) energy profiles along the geodesic[122] interpolated structures of retinal protonated Schiff base with 6 double bonds (PSB6) using optimized structures from Ref. 59, respectively. Calculations were performed by MRSF-TDDFT/cc-pVDZ with BH&HLYP (solid lines), DTCAM-AEE (dashed line), DTCAM-VEE (dotted line). The PESs as calculated by the XMS-CASPT2(12,12)/cc-pVDZ were shown for comparison. The molecular structure and the numbering are shown in the inset.

functionals.

The relevant structures are the all-*trans* and the 11-*cis* and 13-*cis* isomers, where the latter two *cis* geometries can be obtained by the torsions around 11-12 and 13-14 C=C bonds from the all-*trans* conformer, respectively as shown in Fig. 9(a). These isomers are formed via a non-radiative decay through two CIs ($CI_{11-12}$ and $CI_{13-14}$) that exist along the two respective torsional pathways. Park and Shiozaki[59] have shown that the dynamical electron correlations are crucial to properly obtain the relative quantum yields of the two possible pathways. While the XMS-CASPT2 results show that the 11-12 pathway is thermally preferred as the corresponding $CI_{11-12}$ is lower than $CI_{13-14}$, the state average complete active space self-consistent field (SA-CASSCF) predicted the opposite.

Employing rPSB6 optimized geometries at the XMS-CASPT2 level of theory, two geodesic interpolations[122] connecting the 11-*cis* $\rightarrow$ $CI_{11-12}$ $\rightarrow$ all-*trans* as well as 13-*cis* $\rightarrow$ $CI_{13-14}$ $\rightarrow$ all-*trans* were performed. Single point energy calculations by XMS-CASPT2(12,12)/cc-pVDZ were performed on the interpolated points with the Software Bagel,[133] and the results (triangle) are presented in Fig. 9(a) and (b), respectively, where the PESs of MRSF-TDDFT as obtained by the three XC functionals (BH&BHLYP (solid line), DTCAM-AEE (dashed line), and DTCAM-VEE (dotted line)) on the same interpolated geometries are also shown. Regardless of XC functionals, the MRSF-TDDFT results show that $CI_{11-12}$ is lower than $CI_{13-14}$, which is consistent with those of XMS-CASPT2. Furthermore, the exact locations of CIs in terms of torsional angles are also consistent with each other. Among the three functionals, DTCAM-AEE remarkably well reproduced the two-state ($S_0$ and $S_1$) energies of the two *cis* conformers and the two CIs. Even the entire PESs including the barriers in the excited states by DTCAM-AEE are in excellent agreement within $\sim$ 0.3 eV. As the conventional LR-TDDFT is incapable of describing the CIs between $S_1$ and $S_0$, these excellent agreements by MRSF-TDDFT with DTCAM-AEE are quite promising as an alternative to more costly multiconfiguration wavefunction methods, setting a significant milestone toward the understanding of retinal photoisomerizations. As compared to the values by BH&HLYP, those of newly developed DTCAM-AEE and DTCAM-VEE generally produce lower

$S_1$ and $S_0$ energies, making the overall values closer to those of XMS-CASPT2.

# Conclusions

Linear response theories are composed of two consecutive steps of reference self-consistent field (SCF) and response calculations. Typically, a single exchange-correlation (XC) functional is utilized for the entire process. However, it was shown that significant accuracy improvements can be achieved by the "adaptive exact exchange (AEE)" , where different amounts of exact exchange are applied to the two steps respectively. In particular, improvements by a factor of two were observed in the prediction of vertical excitation energies (VEEs), when the exact exchange amount of 50 % is selectively adopted for the response part of calculations in all XC functionals studied in the current paper.

Two new XC functionals, dubbed DTCAM-VEE and DTCAM-AEE, were established for MRSF-TDDFT on the basis of this AEE concept, where the exact exchange contributions for SCF and response parts are individually tuned with the framework of the Coulomb-attenuating XC functional. In the case of DTCAM-VEE, which was mainly tuned for vertical excitation energies (VEEs), its mean absolute errors (MAEs) and interquartile range (IQR) against Thiel's set are as small as 0.218 and 0.327 eV, respectively. On the other hand, in the tuning of DTCAM-AEE functional, the topology of each CI of *trans*-butadiene and thymine, and the timescales of NAMD simulations on thymine were utilized for the correct description of excited state potential energy surfaces. Remarkably, the latter functional yields near-perfect 1/R asymptotic behavior for the charge-transfer states of ethylene-tetrafluoroethylene dimer, which hints at a new way of introducing non-local contributions to the XC functionals. In an application to the challenging retinal protonated Schiff base model systems with six double bonds (rPSB6), which requires non-local XC functionals, the potential energy surfaces of DTCAM-AEE are in excellent agreements with those of extended multi-state second-order complete-active space perturbation theory (XMS-CASPT2), setting a significant milestone toward the understanding of retinal photoisomerizations.

In short, it is demonstrated that a new concept of AEE especially for MRSF-TDDFT with the framework of the Coulomb attenuating scheme exhibits remarkable and promising performances. The current strategy can also be combined with different XC functional schemes and applied to other variants of linear response theories as well, which opens a new direction in the development of XC functionals.

## Acknowledgments

This work was supported by the NRF funded by the Ministry of Science and ICT (2020R1A2C2008246 and 2020R1A5A1019141) Work by S.L. was funded by the US Department of Energy, Office of Science, via Award DE-SC0019374. Work by M.H.-R. was supported by Agence Nationale de la Recherche, Grant number ANR-2021-CE11-0029-03 (Project ULTRArchae).

## Supporting Information Available

A separate supporting information file is provided, which includes the gradient equations, details of NAMD simulations, and additional MAE and Boxplot figures.

## References

(1) Runge, E.; Gross, E. K. Density-functional theory for time-dependent systems. *Phys. Rev. Lett.* **1984**, *52*, 997.

(2) Casida, M. E.; Chong, D. Recent advances in density functional methods. *Computational Chemistry: Reviews of Current Trends* **1995**,

(3) Casida, M. E.; Huix-Rotllant, M. Progress in time-dependent density-functional theory. *Annu. Rev. Phys. Chem.* **2012**, *63*, 287–323.

(4) Dreuw, A.; Weisman, J. L.; Head-Gordon, M. Long-range charge-transfer excited states in time-dependent density functional theory require non-local exchange. *J. Chem. Phys.* **2003**, *119*, 2943–2946.

(5) Dreuw, A.; Head-Gordon, M. Single-reference ab initio methods for the calculation of excited states of large molecules. *Chem. Rev.* **2005**, *105*, 4009–4037.

(6) Dev, P.; Agrawal, S.; English, N. J. Determining the appropriate exchange-correlation functional for time-dependent density functional theory studies of charge-transfer excitations in organic dyes. *J. Chem. Phys.* **2012**, *136*, 224301.

(7) Maitra, N. T. Undoing static correlation: Long-range charge transfer in time-dependent density-functional theory. *J. Chem. Phys.* **2005**, *122*, 234104.

(8) Baerends, E.; Gritsenko, O.; Van Meer, R. The Kohn–Sham gap, the fundamental gap and the optical gap: the physical meaning of occupied and virtual Kohn–Sham orbital energies. *Phys. Chem. Chem. Phys.* **2013**, *15*, 16408–16425.

(9) Cave, R. J.; Zhang, F.; Maitra, N. T.; Burke, K. A dressed TDDFT treatment of the $2^1A_g$ states of butadiene and hexatriene. *Chem. Phys. Lett.* **2004**, *389*, 39–42.

(10) Neugebauer, J.; Baerends, E. J.; Nooijen, M. Vibronic coupling and double excitations in linear response time-dependent density functional calculations: Dipole-allowed states of $N_2$. *J. Chem. Phys.* **2004**, *121*, 6155–6166.

(11) Maitra, N. T.; Zhang, F.; Cave, R. J.; Burke, K. Double excitations within time-dependent density functional theory linear response. *J. Chem. Phys.* **2004**, *120*, 5932–5937.

(12) Park, W.; Shen, J.; Lee, S.; Piecuch, P.; Filatov, M.; Choi, C. H. Internal Conversion between Bright ($1^1B_u^+$) and Dark ($2^1A_g^-$) States in s-trans-Butadiene and s-trans-Hexatriene. *J. Phys. Chem. Lett.* **2021**, *12*, 9720–9729.

(13) Aryasetiawan, F.; Gunnarsson, O.; Rubio, A. Excitation energies from time-dependent density-functional formalism for small systems. *EPL (Europhysics Letters)* **2002**, *57*, 683.

(14) Filatov, M. Ensemble DFT approach to excited states of strongly correlated molecular systems. *Density-functional methods for excited states* **2015**, 97–124.

(15) Levine, B. G.; Ko, C.; Quenneville, J.; Martínez, T. J. Conical intersections and double excitations in time-dependent density functional theory. *Mol. Phys.* **2006**, *104*, 1039–1051.

(16) Huix-Rotllant, M.; Filatov, M.; Gozem, S.; Schapiro, I.; Olivucci, M.; Ferré, N. Assessment of density functional theory for describing the correlation effects on the ground and excited state potential energy surfaces of a retinal chromophore model. *J. Chem. Theory Comput.* **2013**, *9*, 3917–3932.

(17) Gozem, S.; Melaccio, F.; Valentini, A.; Filatov, M.; Huix-Rotllant, M.; Ferré, N.; Frutos, L. M.; Angeli, C.; Krylov, A. I.; Granovsky, A. A. et al. Shape of multireference, equation-of-motion coupled-cluster, and density functional theory potential energy surfaces at a conical intersection. *J. Chem. Theory Comput.* **2014**, *10*, 3074–3084.

(18) Ferré, N.; Filatov, M.; Huix-Rotllant, M. *Density-functional methods for excited states*; Springer, 2016; Vol. 368.

(19) Casanova-Páez, M.; Dardis, M. B.; Goerigk, L. $\omega$B2PLYP and $\omega$B2GPPLYP: the first two double-hybrid density functionals with long-range correction optimized for excitation energies. *J. Chem. Theory Comput.* **2019**, *15*, 4735–4744.

(20) Mester, D.; Kállay, M. Charge-transfer excitations within density functional theory: How accurate are the most recommended approaches? *J. Chem. Theory Comput.* **2022**, *18*, 1646–1662.

(21) Casida, M. E. Propagator corrections to adiabatic time-dependent density-functional theory linear response theory. *J. Chem. Phys.* **2005**, *122*, 054111.

(22) Mester, D.; Kállay, M. Accurate spectral properties within double-hybrid density functional theory: a spin-scaled range-separated second-order algebraic-diagrammatic construction-based approach. *J. Chem. Theory Comput.* **2022**, *18*, 865–882.

(23) Krylov, A. I. Size-consistent wave functions for bond-breaking: The equation-of-motion spin-flip model. *Chem. Phys. Lett.* **2001**, *338*, 375–384.

(24) Li, Z.; Liu, W. Theoretical and numerical assessments of spin-flip time-dependent density functional theory. *J. Chem. Phys.* **2012**, *136*, 024107.

(25) Wang, F.; Ziegler, T. Time-dependent density functional theory based on a noncollinear formulation of the exchange-correlation potential. *J. Chem. Phys.* **2004**, *121*, 12191–12196.

(26) Shao, Y.; Head-Gordon, M.; Krylov, A. I. The spin–flip approach within time-dependent density functional theory: Theory and applications to diradicals. *J. Chem. Phys.* **2003**, *118*, 4807–4818.

(27) Casanova, D.; Krylov, A. I. Spin-flip methods in quantum chemistry. *Phys. Chem. Chem. Phys.* **2020**, *22*, 4326–4342.

(28) Sears, J. S.; Sherrill, C. D.; Krylov, A. I. A spin-complete version of the spin-flip approach to bond breaking: What is the impact of obtaining spin eigenfunctions? *J. Chem. Phys.* **2003**, *118*, 9084–9094.

(29) Mato, J.; Gordon, M. S. A general spin-complete spin-flip configuration interaction method. *Phys. Chem. Chem. Phys.* **2018**, *20*, 2615–2626.

(30) Mato, J.; Gordon, M. S. Analytic non-adiabatic couplings for the spin-flip ORMAS method. *Phys. Chem. Chem. Phys.* **2020**, *22*, 1475–1484.

(31) Zhang, X.; Herbert, J. M. Spin-flip, tensor equation-of-motion configuration interaction with a density-functional correction: A spin-complete method for exploring excited-state potential energy surfaces. *J. Chem. Phys.* **2015**, *143*, 234107.

(32) Lee, S.; Filatov, M.; Lee, S.; Choi, C. H. Eliminating spin-contamination of spin-flip time dependent density functional theory within linear response formalism by the use of zeroth-order mixed-reference (MR) reduced density matrix. *J. Chem. Phys.* **2018**, *149*, 104101.

(33) McWeeny, R.; Sutcliffe, B. *Methods of Molecular Quantum Mechanics*; Academic Press, 1992.

(34) Lee, S.; Kim, E. E.; Nakata, H.; Lee, S.; Choi, C. H. Efficient implementations of analytic energy gradient for mixed-reference spin-flip time-dependent density functional theory (MRSF-TDDFT). *J. Chem. Phys.* **2019**, *150*, 184111.

(35) Lee, S.; Shostak, S.; Filatov, M.; Choi, C. H. Conical Intersections in Organic Molecules: Benchmarking Mixed-Reference Spin–Flip Time-Dependent DFT (MRSF-TD-DFT) vs Spin–Flip TD-DFT. *J. Phys. Chem. A* **2019**, *123*, 6455.

(36) Baek, Y. S.; Lee, S.; Filatov, M.; Choi, C. H. Optimization of Three State Conical Intersections by Adaptive Penalty Function Algorithm in Connection with the Mixed-Reference Spin-Flip Time-Dependent Density Functional Theory Method (MRSF-TDDFT). *J. Phys. Chem. A* **2021**, *125*, 1994–2006.

(37) Kim, H.; Park, W.; Kim, Y.; Filatov, M.; Choi, C. H.; Lee, D. Relief of excited-state antiaromaticity enables the smallest red emitter. *Nat. Commun.* **2021**, *12*, 1–9.

(38) Horbatenko, Y.; Lee, S.; Filatov, M.; Choi, C. H. Performance Analysis and Optimization of Mixed-Reference Spin-Flip Time-Dependent Density Functional Theory (MRSF-TDDFT) for Vertical Excitation Energies and Singlet–Triplet Energy Gaps. *J. Phys. Chem. A* **2019**, *123*, 7991–8000.

(39) Horbatenko, Y.; Sadiq, S.; Lee, S.; Filatov, M.; Choi, C. H. Mixed-Reference Spin-Flip Time-Dependent Density Functional Theory (MRSF-TDDFT) as a Simple yet Accurate Method for Diradicals and Diradicaloids. *J. Chem. Theory Comput.* **2021**, *17*, 848–859.

(40) Lee, S.; Horbatenko, Y.; Filatov, M.; Choi, C. H. Fast and Accurate Computation of Nonadiabatic Coupling Matrix Elements Using the Truncated Leibniz Formula and Mixed-Reference Spin-Flip Time-Dependent Density Functional Theory. *J. Phys. Chem. Lett.* **2021**, *12*, 4722–4728.

(41) Lee, S.; Kim, E.; Lee, S.; Choi, C. H. Fast Overlap Evaluations for Nonadiabatic Molecular Dynamics Simulations: Applications to SF-TDDFT and TDDFT. *J. Chem. Theory Comput.* **2019**, *15*, 882.

(42) Pomogaev, V.; Lee, S.; Shaik, S.; Filatov, M.; Choi, C. H. Exploring Dyson's Orbitals and Their Electron Binding Energies for Conceptualizing Excited States from Response Methodology. *J. Phys. Chem. Lett.* **2021**, *12*, 9963–9972.

(43) Horbatenko, Y.; Lee, S.; Filatov, M.; Choi, C. H. How Beneficial Is the Explicit Account of Doubly-Excited Configurations in Linear Response Theory? *J. Chem. Theory Comput.* **2021**, *17*, 975–984.

(44) Park, W.; Lee, S.; Huix-Rotllant, M.; Filatov, M.; Choi, C. H. Impact of the Dynamic Electron Correlation on the Unusually Long Excited-State Lifetime of Thymine. *J. Phys. Chem. Lett.* **2021**, *12*, 4339–4346.

(45) Lee, S.; Park, W.; Nakata, H.; Filatov, M.; Choi, C. H. Recent advances in ensemble density functional theory and linear response theory for strong correlation. *Bull. Korean Chem. Soc.* **2022**, *43*, 17–34.

(46) Park, W.; Shen, J.; Lee, S.; Piecuch, P.; Joo, T.; Filatov, M.; Choi, C. H. Dual Fluorescence of Octatetraene Hints at a Novel Type of Singlet-to-Singlet Thermally Activated Delayed Fluorescence Process. *J. Phys. Chem. C* **2022**,

(47) Park, W.; Filatov, M.; Sadiq, S.; Gerasimov, I.; Lee, S.; Joo, T.; Choi, C. H. A Plausible Mechanism of Uracil Photohydration Involves an Unusual Intermediate. *J. Phys. Chem. Lett.* **2022**, *13*, 7072–7080.

(48) Huix-Rotllant, M.; Schwinn, K.; Pomogaev, V.; Farmani, M.; Ferré, N.; Lee, S.; Choi, C. H. Photochemistry of thymine in solution and DNA revealed by an electrostatic embedding QM/MM combined with mixed-reference spin-flip TDDFT. *J. Chem. Theory Comput.* **2022**,

(49) Lee, S.; Park, W.; Nakata, H.; Filatov, M.; Choi, C. H. *Time-Dependent Density Functional Theory*; Jenny Stanford Publishing, 2023; pp 101–139.

(50) Shostak, S.; Park, W.; Oh, J.; Kim, J.; Lee, S.; Nam, H.; Filatov, M.; Kim, D.; Choi, C. H. Ultrafast Excited State Aromatization in Dihydroazulene. *J. Am. Chem. Soc.* **2023**,

(51) Sadiq, S.; Park, W.; Mironov, V.; Lee, S.; Filatov, M.; Choi, C. H. Prototropically Controlled Dynamics of Cytosine Photodecay. *J. Phys. Chem. Lett.* **2023**, *14*, 791–797.

(52) Komarov, K.; Park, W.; Lee, S.; Zeng, T.; Choi, C. H. Accurate Spin–Orbit Coupling by Relativistic Mixed-Reference Spin-Flip-TDDFT. *J. Chem. Theory Comput.* **2023**, *19*, 953–964.

(53) Park, W.; Alías-Rodríguez, M.; Cho, D.; Lee, S.; Huix-Rotllant, M.; Choi, C. H. Mixed-reference spin-flip time-dependent density functional theory for accurate x-ray absorption spectroscopy. *J. Chem. Theory Comput.* **2022**, *18*, 6240–6250.

(54) Japahuge, A.; Lee, S.; Choi, C. H.; Zeng, T. Design of singlet fission chromophores with cyclic (alkyl)(amino) carbene building blocks. *J. Chem. Phys.* **2019**, *150*, 234306.

(55) Pradhan, E.; Lee, S.; Choi, C. H.; Zeng, T. Diboron-and diaza-doped anthracenes and phenanthrenes: their electronic structures for being singlet fission chromophores. *J. Phys. Chem. A* **2020**, *124*, 8159–8172.

(56) James, D.; Pradhan, E.; Lee, S.; Choi, C. H.; Zeng, T. Dicarbonyl anthracenes and phenanthrenes as singlet fission chromophores. *Can. J. Chem.* **2022**, *99*, 1–10.

(57) Barca, G. M. J.; Bertoni, C.; Carrington, L.; Datta, D.; De Silva, N.; Deustua, J. E.; Fedorov, D. G.; Gour, J. R.; Gunina, A. O.; Guidez, E. et al. Recent developments in

the general atomic and molecular electronic structure system. *J. Chem. Phys.* **2020**, *152*, 154102.

(58) Huix-Rotllant, M.; Natarajan, B.; Ipatov, A.; Wawire, C. M.; Deutsch, T.; Casida, M. E. Assessment of noncollinear spin-flip Tamm–Dancoff approximation time-dependent density-functional theory for the photochemical ring-opening of oxirane. *Phys. Chem. Chem. Phys.* **2010**, *12*, 12811–12825.

(59) Park, J. W.; Shiozaki, T. On the accuracy of retinal protonated Schiff base models. *Mol. Phys.* **2018**, *116*, 2583–2590.

(60) Dreuw, A.; Head-Gordon, M. Failure of time-dependent density functional theory for long-range charge-transfer excited states: the zincbacteriochlorin- bacteriochlorin and bacteriochlorophyll- spheroidene complexes. *J. Am. Chem. Soc.* **2004**, *126*, 4007–4016.

(61) Zhang, Y.; Xu, X.; Goddard III, W. A. Doubly hybrid density functional for accurate descriptions of nonbond interactions, thermochemistry, and thermochemical kinetics. *Proc. Natl. Acad. Sci. U.S.A.* **2009**, *106*, 4963–4968.

(62) Schreiber, M.; Silva-Junior, M. R.; Sauer, S. P.; Thiel, W. Benchmarks for electronically excited states: CASPT2, CC2, CCSD, and CC3. *J. Chem. Phys.* **2008**, *128*, 134110.

(63) Boese, A. D.; Handy, N. C. A new parametrization of exchange–correlation generalized gradient approximation functionals. *J. Chem. Phys.* **2001**, *114*, 5497–5503.

(64) Wang, Y.; Jin, X.; Yu, H. S.; Truhlar, D. G.; He, X. Revised M06-L functional for improved accuracy on chemical reaction barrier heights, noncovalent interactions, and solid-state physics. *Proc. Natl. Acad. Sci. U.S.A.* **2017**, *114*, 8487–8492.

(65) Baker, J.; Pulay, P. Assessment of the Handy–Cohen optimized exchange density functional for organic reactions. *J. Chem. Phys.* **2002**, *117*, 1441–1449.

(66) Furness, J. W.; Kaplan, A. D.; Ning, J.; Perdew, J. P.; Sun, J. Accurate and numerically efficient r2SCAN meta-generalized gradient approximation. *J. Phys. Chem. Lett.* **2020**, *11*, 8208–8215.

(67) Holzwarth, N.; Torrent, M.; Charraud, J.-B.; Côté, M. Cubic spline solver for generalized density functional treatments of atoms and generation of atomic datasets for use with exchange-correlation functionals including meta-GGA. *Phys. Rev. B* **2022**, *105*, 125144.

(68) Slater, J. C.; Phillips, J. C. Quantum Theory of Molecules and Solids Vol. 4: The Self-Consistent Field for Molecules and Solids. *Phys. Today* **1974**, *27*, 49–50.

(69) Vosko, S. H.; Wilk, L.; Nusair, M. Accurate spin-dependent electron liquid correlation energies for local spin density calculations: a critical analysis. *Can. J. Phys.* **1980**, *58*, 1200–1211.

(70) Boese, A. D.; Handya, N. C. New exchange-correlation density functionals: The role of the kinetic-energy density. *exchange* **2002**, *1*, 2.

(71) Staroverov, V. N.; Scuseria, G. E.; Tao, J.; Perdew, J. P. Comparative assessment of a new nonempirical density functional: Molecules and hydrogen-bonded complexes. *J. Chem. Phys.* **2003**, *119*, 12129–12137.

(72) Chai, J.-D.; Head-Gordon, M. Systematic optimization of long-range corrected hybrid density functionals. *J. Chem. Phys.* **2008**, *128*.

(73) Jensen, K. P. Bioinorganic chemistry modeled with the TPSSh density functional. *Inorg. Chem.* **2008**, *47*, 10357–10365.

(74) Yanai, T.; Tew, D. P.; Handy, N. C. A new hybrid exchange–correlation functional using the Coulomb-attenuating method (CAM-B3LYP). *Chem. Phys. Lett.* **2004**, *393*, 51–57.

(75) Shao, Y.; Mei, Y.; Sundholm, D.; Kaila, V. R. Benchmarking the performance of

time-dependent density functional theory methods on biochromophores. *J. Chem. Theory Comput.* **2019**, *16*, 587–600.

(76) Becke, A. D. Density-functional thermochemistry. V. Systematic optimization of exchange-correlation functionals. *J. Chem. Phys.* **1997**, *107*, 8554–8560.

(77) Schmider, H. L.; Becke, A. D. Optimized density functionals from the extended G2 test set. *J. Chem. Phys.* **1998**, *108*, 9624–9631.

(78) Becke, A. D. Density-functional exchange-energy approximation with correct asymptotic behavior. *Phys. Rev. A* **1988**, *38*, 3098.

(79) Becke, A. D. A new mixing of Hartree–Fock and local density-functional theories. *J. Chem. Phys.* **1993**, *98*, 1372–1377.

(80) Lee, C.; Yang, W.; Parr, R. G. Development of the Colle-Salvetti correlation-energy formula into a functional of the electron density. *Phys. Rev. B* **1988**, *37*, 785.

(81) Perdew, J. P.; Chevary, J. A.; Vosko, S. H.; Jackson, K. A.; Pederson, M. R.; Singh, D. J.; Fiolhais, C. Atoms, molecules, solids, and surfaces: Applications of the generalized gradient approximation for exchange and correlation. *Phys. Rev. B* **1992**, *46*, 6671.

(82) Xu, X.; Goddard III, W. A. The X3LYP extended density functional for accurate descriptions of nonbond interactions, spin states, and thermochemical properties. *Proc. Natl. Acad. Sci. U.S.A.* **2004**, *101*, 2673–2677.

(83) Austin, A.; Petersson, G. A.; Frisch, M. J.; Dobek, F. J.; Scalmani, G.; Throssell, K. A density functional with spherical atom dispersion terms. *J. Chem. Theory Comput.* **2012**, *8*, 4989–5007.

(84) Deák, P.; Aradi, B.; Frauenheim, T.; Janzén, E.; Gali, A. Accurate defect levels obtained from the HSE06 range-separated hybrid functional. *Phys. Rev. B* **2010**, *81*, 153203.

(85) Adamo, C.; Barone, V. Toward reliable density functional methods without adjustable parameters: The PBE0 model. *J. Chem. Phys.* **1999**, *110*, 6158–6170.

(86) Verma, P.; Bartlett, R. J. Increasing the applicability of density functional theory. IV. Consequences of ionization-potential improved exchange-correlation potentials. *J. Chem. Phys.* **2014**, *140*.

(87) Zhao, Y.; Truhlar, D. G. The M06 suite of density functionals for main group thermochemistry, thermochemical kinetics, noncovalent interactions, excited states, and transition elements: two new functionals and systematic testing of four M06-class functionals and 12 other functionals. *Theor. Chem. Acc.* **2008**, *120*, 215–241.

(88) Savin, A.; Umrigar, C. J.; Gonze, X. Relationship of Kohn–Sham eigenvalues to excitation energies. *Chem. Phys. Lett.* **1998**, *288*, 391–395.

(89) Gritsenko, O.; Baerends, E. J. Asymptotic correction of the exchange–correlation kernel of time-dependent density functional theory for long-range charge-transfer excitations. *J. Chem. Phys.* **2004**, *121*, 655–660.

(90) Domcke, W., Yarkony, D. R., Köppel, H., Eds. *Conical Intersections. Electronic Structure, Dynamics and Spectroscopy*; Advanced series in physical chemistry; World Scientific: Singapore, 2004; Vol. 15.

(91) Domcke, W., Yarkony, D. R., Köppel, H., Eds. *Conical Intersections. Theory, Computation and Experiment*; Advanced series in physical chemistry; World Scientific: Singapore, 2011; Vol. 17.

(92) Hudson, B.; Kohler, B. A low-lying weak transition in the polyene $\alpha,\omega$-diphenyloctatetraene. *Chem. Phys. Lett.* **1972**, *14*, 299–304.

(93) Schulten, K.; Karplus, M. On the origin of a low-lying forbidden transition in polyenes and related molecules. *Chem. Phys. Lett.* **1972**, *14*, 305–309.

(94) Hudson, B.; Kohler, B. Electronic structure and spectra of finite linear polyenes. *Synth. Metals* **1984**, *9*, 241–253, Proceedings of the Workshop "Synthetic Metals II".

(95) Pariser, R. Theory of the electronic spectra and structure of the polyacenes and of alternant hydrocarbons. *J. Chem. Phys.* **1956**, *24*, 250–268.

(96) Bahnick, D. A. Use of Huckel Molecular Orbital Theory in Interpreting the Visible Spectra of Polymethine Dyes: An Undergraduate Physical Chemistry Experiment. *J. Chem. Educ.* **1994**, *71*, 171.

(97) Hellmann, H. *Einführung in die Quantenchemie*; Franz Deuticke: Leipzig, 1937; p 285.

(98) Herndon, W. C.; Silber, E. Simplified molecular orbitals for organic molecules. *J. Chem. Educ.* **1971**, *48*, 502.

(99) Baker, A. D.; Baker, M. D. A geometric method for determining the Huckel molecular orbital energy levels of open chain, fully conjugated molecules. *J. Chem. Educ.* **1984**, *61*, 770.

(100) Tavan, P.; Schulten, K. The low-lying electronic excitations in long polyenes: A PPP-MRD-CI study. *J. Chem. Phys.* **1986**, *85*, 6602–6609.

(101) Fuß, W.; Lochbrunner, S.; Müller, A.; Schikarski, T.; Schmid, W.; Trushin, S. Pathway approach to ultrafast photochemistry: potential surfaces, conical intersections and isomerizations of small polyenes. *Chem. Phys.* **1998**, *232*, 161–174.

(102) Fuß, W.; Haas, Y.; Zilberg, S. Twin states and conical intersections in linear polyenes. *Chem. Phys.* **2000**, *259*, 273–295.

(103) Fuß, W.; Schmid, W.; Trushin, S. Ultrafast electronic relaxation of s-trans-butadiene. *Chem. Phys. Lett.* **2001**, *342*, 91–98.

(104) Levine, B. G.; Martínez, T. J. Ab initio multiple spawning dynamics of excited butadiene: Role of charge transfer. *J. Phys. Chem. A* **2009**, *113*, 12815–12824.

(105) Götze, J. P. Vibrational Relaxation in Carotenoids as an Explanation for Their Rapid Optical Properties. *J. Phys. Chem. B* **2019**, *123*, 2203–2209.

(106) Yamazaki, S.; Taketsugu, T. Nonradiative deactivation mechanisms of uracil, thymine, and 5-fluorouracil: A comparative ab initio study. *J. Phys. Chem. A* **2012**, *116*, 491–503.

(107) Perun, S.; Sobolewski, A. L.; Domcke, W. Conical intersections in thymine. *J. Phys. Chem. A* **2006**, *110*, 13238–13244.

(108) Stojanović, L.; Bai, S.; Nagesh, J.; Izmaylov, A.; Crespo-Otero, R.; Lischka, H.; Barbatti, M. New Insights into the State Trapping of UV-Excited Thymine. *Molecules* **2016**, *21*, 1603.

(109) Hudock, H. R.; Levine, B. G.; Thompson, A. L.; Satzger, H.; Townsend, D.; Gador, N.; Ullrich, S.; Stolow, A.; Martinez, T. J. Ab initio molecular dynamics and time-resolved photoelectron spectroscopy of electronically excited uracil and thymine. *J. Phys. Chem. A* **2007**, *111*, 8500–8508.

(110) Yu, H.; Sanchez-Rodriguez, J. A.; Pollum, M.; Crespo-Hernández, C. E.; Mai, S.; Marquetand, P.; González, L.; Ullrich, S. Internal conversion and intersystem crossing pathways in UV excited, isolated uracils and their implications in prebiotic chemistry. *Phys. Chem. Chem. Phys.* **2016**, *18*, 20168–20176.

(111) Kang, H.; Lee, K. T.; Jung, B.; Ko, Y. J.; Kim, S. K. Intrinsic lifetimes of the excited state of DNA and RNA bases. *J. Am. Chem. Soc.* **2002**, *124*, 12958–12959.

(112) Ullrich, S.; Schultz, T.; Zgierski, M. Z.; Stolow, A. Electronic relaxation dynamics in DNA and RNA bases studied by time-resolved photoelectron spectroscopy. *Phys. Chem. Chem. Phys.* **2004**, *6*, 2796–2801.

(113) McFarland, B. K.; Farrell, J. P.; Miyabe, S.; Tarantelli, F.; Aguilar, A.; Berrah, N.;

Bostedt, C.; Bozek, J. D.; Bucksbaum, P. H.; Castagna, J. C. et al. Ultrafast X-ray Auger probing of photoexcited molecular dynamics. *Nat. Commun.* **2014**, *5*, 4235.

(114) González-Vázquez, J.; González, L.; Samoylova, E.; Schultz, T. Thymine relaxation after UV irradiation: the role of tautomerization and $\pi\sigma^*$ states. *Phys. Chem. Chem. Phys.* **2009**, *11*, 3927–3934.

(115) Gador, N.; Samoylova, E.; Smith, V. R.; Stolow, A.; Rayner, D. M.; Radloff, W.; Hertel, I. V.; Schultz, T. Electronic structure of adenine and thymine base pairs studied by femtosecond electron- ion coincidence spectroscopy. *J. Phys. Chem. A* **2007**, *111*, 11743–11749.

(116) Canuel, C.; Mons, M.; Piuzzi, F.; Tardivel, B.; Dimicoli, I.; Elhanine, M. Excited states dynamics of DNA and RNA bases: Characterization of a stepwise deactivation pathway in the gas phase. *J. Chem. Phys.* **2005**, *122*, 074316.

(117) Samoylova, E.; Schultz, T.; Hertel, I. V.; Radloff, W. Analysis of ultrafast relaxation in photoexcited DNA base pairs of adenine and thymine. *Chem. Phys.* **2008**, *347*, 376–382.

(118) Ligare, M.; Siouri, F.; Bludsky, O.; Nachtigallova, D.; de Vries, M. S. Characterizing the dark state in thymine and uracil by double resonant spectroscopy and quantum computation. *Phys. Chem. Chem. Phys.* **2015**, *17*, 24336–24341.

(119) Samoylova, E.; Lippert, H.; Ullrich, S.; Hertel, I. V.; Radloff, W.; Schultz, T. Dynamics of photoinduced processes in adenine and thymine base pairs. *J. Am. Chem. Soc.* **2005**, *127*, 1782–1786.

(120) Wolf, T. J. A.; Myhre, R. H.; Cryan, J. P.; Coriani, S.; Squibb, R. J.; Battistoni, A.; Berrah, N.; Bostedt, C.; Bucksbaum, P.; Coslovich, G. et al. Probing ultrafast $\pi\pi^*/n\pi^*$ internal conversion in organic chromophores via K-edge resonant absorption. *Nat. Commun.* **2017**, *8*, 29.

(121) Miura, Y.; Yamamoto, Y.-i.; Karashima, S.; Orimo, N.; Hara, A.; Fukuoka, K.; Ishiyama, T.; Suzuki, T. Formation of Long-Lived Dark States during Electronic Relaxation of Pyrimidine Nucleobases Studied Using Extreme Ultraviolet Time-Resolved Photoelectron Spectroscopy. *J. Am. Chem. Soc.* **2023**, *145*, 3369–3381.

(122) Zhu, X.; Thompson, K. C.; Martínez, T. J. Geodesic interpolation for reaction pathways. *J. Chem. Phys.* **2019**, *150*, 164103.

(123) Kiefer, H. V.; Gruber, E.; Langeland, J.; Kusochek, P. A.; Bochenkova, A. V.; Andersen, L. H. Intrinsic photoisomerization dynamics of protonated Schiff-base retinal. *Nat. Commun.* **2019**, *10*, 1210.

(124) Liu, L.; Liu, J.; Martinez, T. J. Dynamical correlation effects on photoisomerization: Ab initio multiple spawning dynamics with MS-CASPT2 for a model trans-protonated Schiff base. *J. Phys. Chem. B* . **2016**, *120*, 1940–1949.

(125) Zhang, X.; Herbert, J. M. Nonadiabatic dynamics with spin-flip vs linear-response time-dependent density functional theory: A case study for the protonated Schiff base C5H6NH2+. *J. Chem. Phys.* **2021**, *155*.

(126) Zhou, P.; Liu, J.; Han, K.; He, G. The photoisomerization of 11-cis-retinal protonated schiff base in gas phase: Insight from spin-flip density functional theory. *J. Comput. Chem.* **2014**, *35*, 109–120.

(127) Gozem, S.; Huntress, M.; Schapiro, I.; Lindh, R.; Granovsky, A. A.; Angeli, C.; Olivucci, M. Dynamic Electron Correlation Effects on the Ground State Potential Energy Surface of a Retinal Chromophore Model. *J. Chem. Theory Comput.* **2012**, *8*, 4069–4080.

(128) Gozem, S.; Krylov, A. I.; Olivucci, M. Conical Intersection and Potential Energy Surface Features of a Model Retinal Chromophore: Comparison of EOM-CC and Multireference Methods. *J. Chem. Theory Comput.* **2013**, *9*, 284–292.

(129) Gozem, S.; Melaccio, F.; Lindh, R.; Krylov, A. I.; Granovsky, A. A.; Angeli, C.; Olivucci, M. Mapping the Excited State Potential Energy Surface of a Retinal Chromophore Model with Multireference and Equation-of-Motion Coupled-Cluster Methods. *J. Chem. Theory Comput.* **2013**, *9*, 4495–4506.

(130) Xu, X.; Gozem, S.; Olivucci, M.; Truhlar, D. G. Combined Self-Consistent-Field and Spin-Flip Tamm–Dancoff Density Functional Approach to Potential Energy Surfaces for Photochemistry. *J. Phys. Chem. Lett.* **2013**, *4*, 253–258.

(131) Tuna, D.; Lefrancois, D.; Wolanéski, Ł.; Gozem, S.; Schapiro, I.; Andruniów, T.; Dreuw, A.; Olivucci, M. Assessment of Approximate Coupled-Cluster and Algebraic-Diagrammatic-Construction Methods for Ground-and Excited-State Reaction Paths and the Conical-Intersection Seam of a Retinal-Chromophore Model. *J. Chem. Theory Comput.* **2015**, *11*, 5758–5781.

(132) Zen, A.; Coccia, E.; Gozem, S.; Olivucci, M.; Guidoni, L. Quantum Monte Carlo Treatment of the Charge Transfer and Diradical Electronic Character in a Retinal Chromophore Minimal Model. *J. Chem. Theory Comput.* **2015**, *11*, 992–1005.

(133) Shiozaki, T. BAGEL: brilliantly advanced general electronic-structure library. *Wiley Interdiscip. Rev. Comput. Mol. Sci.* **2018**, *8*, e1331.